A&A 677, A57 (2023)
https://doi.org/10.1051/0004-6361/202347088

Astronomy & Astrophysics

Complex variations in X-ray polarization in the X-ray pulsar LS V +44 17/RX J0440.9+4431

Victor Doroshenko[1], Juri Poutanen[2], Jeremy Heyl[3], Sergey S. Tsygankov[2], Ilaria Caiazzo[4], Roberto Turolla[5,6], Alexandra Veledina[2,7], Martin C. Weisskopf[8], Sofia V. Forsblom[2], Denis González-Caniulef[9], Vladislav Loktev[2], Christian Malacaria[10], Alexander A. Mushtukov[11], Valery F. Suleimanov[1], Alexander A. Lutovinov[12], Ilya A. Mereminskiy[12], Sergey V. Molkov[12], Alexander Salganik[13,12], Andrea Santangelo[1], Andrei V. Berdyugin[2], Vadim Kravtsov[2], Anagha P. Nitindala[2], Iván Agudo[14], Lucio A. Antonelli[15,16], Matteo Bachetti[17], Luca Baldini[18,19], Wayne H. Baumgartner[8], Ronaldo Bellazzini[18], Stefano Bianchi[20], Stephen D. Bongiorno[8], Raffaella Bonino[21,22], Alessandro Brez[18], Niccolò Bucciantini[23,24,25], Fiamma Capitanio[29], Simone Castellano[18], Elisabetta Cavazzuti[26], Chien-Ting Chen[27], Stefano Ciprini[28,16], Enrico Costa[29], Alessandra De Rosa[29], Ettore Del Monte[29], Laura Di Gesu[26], Niccolò Di Lalla[30], Alessandro Di Marco[29], Immacolata Donnarumma[26], Michal Dovčiak[31], Steven R. Ehlert[8], Teruaki Enoto[32], Yuri Evangelista[29], Sergio Fabiani[29], Riccardo Ferrazzoli[29], Javier A. García[33], Shuichi Gunji[34], Kiyoshi Hayashida[35,†], Wataru Iwakiri[36], Svetlana G. Jorstad[37,13], Philip Kaaret[8], Vladimir Karas[31], Fabian Kislat[38], Takao Kitaguchi[32], Jeffery J. Kolodziejczak[8], Henric Krawczynski[39], Fabio La Monaca[29], Luca Latronico[21], Ioannis Liodakis[40], Simone Maldera[21], Alberto Manfreda[41], Frédéric Marin[42], Andrea Marinucci[26], Alan P. Marscher[37], Herman L. Marshall[43], Francesco Massaro[21,22], Giorgio Matt[20], Ikuyuki Mitsuishi[44], Tsunefumi Mizuno[45], Fabio Muleri[29], Michela Negro[46,47,48], Chi-Yung Ng[49], Stephen L. O'Dell[8], Nicola Omodei[30], Chiara Oppedisano[21], Alessandro Papitto[15], George G. Pavlov[50], Abel L. Peirson[30], Matteo Perri[16,15], Melissa Pesce-Rollins[18], Pierre-Olivier Petrucci[51], Maura Pilia[17], Andrea Possenti[17], Simonetta Puccetti[16], Brian D. Ramsey[8], John Rankin[29], Ajay Ratheesh[29], Oliver J. Roberts[27], Roger W. Romani[30], Carmelo Sgrò[18], Patrick Slane[52], Paolo Soffitta[29], Gloria Spandre[18], Douglas A. Swartz[27], Toru Tamagawa[32], Fabrizio Tavecchio[53], Roberto Taverna[5], Yuzuru Tawara[44], Allyn F. Tennant[8], Nicholas E. Thomas[8], Francesco Tombesi[54,28,55], Alessio Trois[17], Jacco Vink[56], Kinwah Wu[6], Fei Xie[57,29], and Silvia Zane[6]

(Affiliations can be found after the references)

Received 3 June 2023 / Accepted 30 June 2023

ABSTRACT

We report on Imaging X-ray polarimetry explorer (IXPE) observations of the Be-transient X-ray pulsar LS V +44 17/RX J0440.9+4431 made at two luminosity levels during the giant outburst in January–February 2023. Considering the observed spectral variability and changes in the pulse profiles, the source was likely caught in supercritical and subcritical states with significantly different emission-region geometry, associated with the presence of accretion columns and hot spots, respectively. We focus here on the pulse-phase-resolved polarimetric analysis and find that the observed dependencies of the polarization degree and polarization angle (PA) on the pulse phase are indeed drastically different for the two observations. The observed differences, if interpreted within the framework of the rotating vector model (RVM), imply dramatic variations in the spin axis inclination, the position angle, and the magnetic colatitude by tens of degrees within the space of just a few days. We suggest that the apparent changes in the observed PA phase dependence are predominantly related to the presence of an unpulsed polarized component in addition to the polarized radiation associated with the pulsar itself. We then show that the observed PA phase dependence in both observations can be explained with a single set of RVM parameters defining the pulsar's geometry. We also suggest that the additional polarized component is likely produced by scattering of the pulsar radiation in the equatorial disk wind.

Key words. accretion, accretion disks – magnetic fields – pulsars: individual: RX J0440.9+4431 – stars: neutron – X-rays: binaries

1. Introduction

The Be/X-ray binary (BeXRB) LS V +44 17/RX J0440.9+4431 was discovered and identified as a candidate X-ray binary at ~3.2 kpc in the ROSAT survey (Motch et al. 1997). The discovery of hard X-ray emission and pulsations with a period of about 206 s confirmed the source is an X-ray pulsar (XRP, Reig & Roche 1999). The properties of the optical counterpart were investigated in detail by Reig et al. (2005), who classified it as a Be star of class B0.2V and reported on brightness and Hα line profile variability typical for this class of sources. Reig et al. (2005) also estimated the distance to the source as being around 3.3 kpc; this has recently been revised to 2.4 ± 0.1 kpc based on *Gaia* DR3 data (Bailer-Jones et al. 2021).

Properties of the binary remain relatively unexplored in the X-ray band as only a few relatively faint Type I outbursts typical

† Deceased.

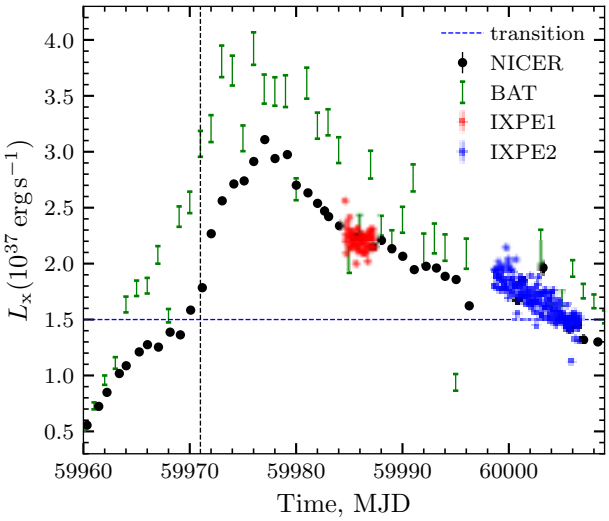

Fig. 1. Light curve of the 2023 outburst of RX J0440.9+4431 as observed by the facilities indicated in the legend and described in the main text. The vertical dashed line marks the probable date of the transition to a supercritical regime (around MJD 59971, i.e., January 27, 2023), while the horizontal dashed line marks the approximate luminosity level at the transition.

for Be X-ray binaries have been observed up to now (Morii et al. 2010; Tsygankov et al. 2012; Ferrigno et al. 2013). Besides the outburst activity typical for BeXRBs, LS V +44 17 is also known for being one of the few systems in which accretion continues during quiescence, in this case at the X-ray luminosity $L_X \sim (1.5–4) \times 10^{34}$ erg s^{-1} (Reig & Roche 1999; La Palombara et al. 2012). We note that, considering the observed spin period and luminosity, the accretion in quiescence is likely powered by a cold, non-ionized disk (Tsygankov et al. 2017), although wind accretion cannot be excluded.

The transient was mainly active in 2010 and 2011 (Morii et al. 2010; Finger & Camero-Arranz 2010; Tsygankov et al. 2012; Ferrigno et al. 2013), reaching peak luminosities of $(1–5) \times 10^{36}$ erg s^{-1} (here and below we adopt the revised distance estimate of 2.4 kpc). Based on observations during this time, a tentative orbital period of ∼150 d and the presence of a cyclotron line at ∼30 keV, implying a magnetic field of $B \sim 3 \times 10^{12}$ G, have been reported by Tsygankov et al. (2012). No evidence for such a feature was, however, found by Ferrigno et al. (2013) using the same data and observations of the 2011 outburst. The reported pulse profiles were relatively simple and almost sine-like throughout the 0.3–60 keV energy range, although some luminosity-dependent structures can be identified in the 3–15 keV range, where counting statistics are highest (Tsygankov et al. 2012). In particular, a relatively sharp dip following the main peak also reported by Usui et al. (2012) can be noted. This has been interpreted as obscuration of the emission region by the accretion stream. The relatively low observed luminosity and a rather simple pulse-profile shape indicate that during these observations the source likely resided in the subcritical accretion regime, when the emission came directly from a hotspot and not from an accretion column expected to arise at higher luminosities (Basko & Sunyaev 1976). On the other hand, Ferrigno et al. (2013) investigated in detail the evolution of the spectral energy distribution with luminosity and conclude that the spectral curvature observed at the highest luminosities may be attributed to the transition to a radiative-pressure-dominated accretion regime and the onset of an accretion column at $L_X \sim 2 \times 10^{36}$ erg s^{-1}, which they argue is consistent with theoretic expectations assuming the magnetic field strength estimated from the observed cyclotron line energy. We conclude thus that there are no solid constraints on either the magnetic field or the emission-region geometry for this object.

Most recently RX J0440.9+4431 became active in December 2022 (Nakajima et al. 2022) when another Type I outburst similar to those in 2010–2011 was observed. The source then entered a giant outburst phase in January–February 2023, peaking at a luminosity of $\sim 4 \times 10^{37}$ erg s^{-1} (Pal et al. 2023; Salganik et al. 2023a), several times brighter than previously observed. Extensive monitoring by several facilities, including *NuSTAR* and NICER, allowed Coley et al. (2023) and Salganik et al. (2023b) to detect transitions in the spectral and timing properties of the source around MJD 59971 (January 27, 2023) and MJD 59995 (February 20, 2023). These are shown in Fig. 1 and interpreted by Salganik et al. (2023b) as marking the transition to and from a supercritical accretion regime. Here we focus on the results obtained with the Imaging X-ray Polarimeter Explorer (IXPE, Weisskopf et al. 2022), which observed the source in both states. With the launch of IXPE, X-ray polarimetry became a new observational window to study accreting XRPs. It can be used to obtain independent constraints on their geometrical parameters through pulse-phase-resolved polarimetric analysis, which is the main objective of the current work.

The paper is organized as follows. In Sect. 2, we provide a summary of the observations used and briefly discuss the analysis procedures adopted. In Sect. 3 we discuss the IXPE results in more detail and put them in the context of the results of outburst monitoring by NICER. We modeled the data, provide constraints on the pulsar's geometry, and discuss the broader implications of the results in Sect. 4. We summarize our findings in Sect. 5.

2. Observations and data analysis

IXPE observed the source twice, at flux levels that differed by a factor of two. The first observation (Obs. 1), with ObsID 02250401, was carried out between MJD 59984.65–59987.40 (132 ks effective exposure, with around 3.8 M source counts in the 2–8 keV band in total). The second observation (Obs. 2), with ObsID 02250501, was carried out between MJD 59998.66–60006.66 (373 ks effective exposure, with 8.3 M source counts in total). We also used NICER observations complemented with *Fermi*/Gamma-ray Burst Monitor (GBM) measurements of source spin frequency (Malacaria et al. 2020) to characterize the evolution of the soft pulse profile shape over the outburst in order to ensure accurate absolute pulse-phase alignment of the IXPE data. Finally, we made use of the *Swift*/BAT 15–50 keV light curve[1]. In the following section, we briefly describe relevant properties, analysis procedures, and the results for each instrument.

2.1. IXPE

The IXPE is a joint mission of NASA and the Italian Space Agency launched on December 9, 2021. It consists of three identical grazing-incidence telescope and detector modules operating in the 2–8 keV energy band. Each telescope comprises an X-ray mirror assembly and a polarization-sensitive detector unit equipped with a gas-pixel detector (Soffitta et al. 2021; Baldini et al. 2021), and provides imaging polarimetry with a

[1] https://swift.gsfc.nasa.gov/results/transients/weak/LSVp4417/

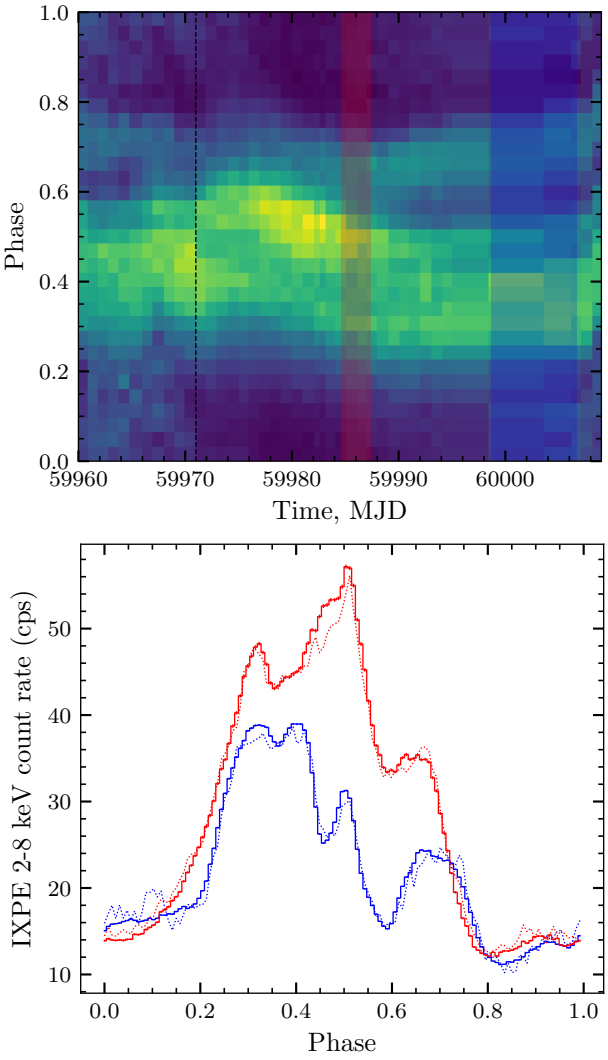

Fig. 2. Evolution of the pulse profiles during the outburst. Top: color-coded normalized pulse profiles as observed by NICER. Slices in the vertical direction correspond to pulse profiles in individual NICER observations, the shaded strips mark the times of IXPE observations, and the vertical dashed line is the same as in Fig. 1. Bottom: pulse profiles in the 2−8 keV band observed by IXPE in two observations (histogram) and NICER during the same period (dotted line, scaled to match the IXPE count rate).

time resolution better than 10 µs over the detector-limited field of view of 12′.9 × 12′.9. A detailed description of the observatory and its performance is given in Weisskopf et al. (2022). The Level 2 data were processed with the IXPEOBSSIM package (Baldini et al. 2022) version 30.2.3[2] using the Calibration database released on November 17, 2022 (v12). Source photons were collected from a circular region with a radius $R_{\rm src}$ of 1′.6 centered on the source position determined by fitting a Gaussian function to the raw count map. The background appears to be negligible in both observations (a typical background count rate from a region of the same size in the 2−8 keV band of IXPE is ∼0.02 count s^{-1} and the observed source count rate is ≥10 count s^{-1} at all times), and thus its contribution was ignored in the analysis (Di Marco et al. 2023). Taking into account the high number of source counts even in individual phase bins and the low background level, we also did not employ track weighing or acceptance corrections.

Table 1. Pulsar ephemerides for the two IXPE observations.

Parameter	IXPE1	IXPE2
T_0 (MJD)	59 984.64718	59 998.65768
ν (mHz)	4.8484 (8)	4.8670 (1)
$\dot{\nu}$ (s^{-2})	$3\,(2)\times10^{-11}$	$1.42\,(3)\times10^{-11}$
$\ddot{\nu}$ (s^{-3})	$-1\,(2)\times10^{-16}$	$-8\,(1)\times10^{-18}$

Notes. The uncertainties are reported at a 1σ confidence level. The reference epoch, T_0, is fixed to the arrival time of the first pulse.

For the timing analysis, the photons' arrival times were corrected to the Solar System barycenter using the `barycorr` task. No binary correction was done as at the time of writing the orbital parameters of the system were still not known. The pulsar ephemerides were then obtained for each of the IXPE observations using the phase-connection technique (Deeter et al. 1981) and are reported in Table 1. The absolute phase alignment between the two IXPE observations was done using the peak at around phase 0.5, which appears to be present throughout most of the outburst, as indicated by NICER monitoring and discussed below. The ephemerides were then used directly to either produce pulse profiles or to generate a set of good-time-interval (GTI) files to define the phase intervals for pulse-phase-resolved analysis. Using the `pcube` routine in IXPEOBSSIM (Baldini et al. 2022) in a broad 2−8 keV band, we extracted binned Stokes parameters I, Q, and U (Kislat et al. 2015), taking the modulation factor of the instrument into account. We define normalized Stokes parameters as $q = Q/I$ and $u = U/I$. The polarization degree (PD) and the polarization angle (PA) can be obtained using standard formulae: PD = $\sqrt{q^2+u^2}$ and PA = $\frac{1}{2}\arctan(u/q)$.

2.2. NICER

In addition to absolute phasing, monitoring of pulse profile shape changes can also be a useful probe for possible changes in the accretion regime associated with the onset of an accretion column (Reig & Nespoli 2013; Wilson-Hodge et al. 2018; Doroshenko et al. 2020), and put the snapshot IXPE observations in a broader context. All available NICER observations were processed using the `nicerl2` task, and then light curves in the 1−10, 4−7, and 7−10 keV energy bands were extracted using the `nicerl3-lc` script. The extracted light curves were then corrected to the Solar System barycenter and folded, assuming a single-phase model based on the spin-frequency measurements of the source done by *Fermi*/GBM[3] as follows. First, we interpolated raw frequency measurements to obtain a smooth function characterizing the frequency evolution of the source with time. This interpolated function was then used to calculate the absolute phase of each pulse within the period covered by the observations. That is, the arrival time of each subsequent pulse was calculated using the arrival time and local frequency of the previous one (for the first pulse, the phase was set arbitrarily). Finally, we calculated a reference epoch and folding frequency for each of the NICER observations using the obtained interpolated functions. The reference phase was selected such that the narrow peak at phase ∼0.5 visible in both IXPE observations occurs at the same phase as in simultaneous NICER data. The result

[2] https://github.com/lucabaldini/ixpeobssim

[3] https://gammaray.nsstc.nasa.gov/gbm/science/pulsars/lightcurves/rxj0440.html

presented in Fig. 2 exhibits no major regular phase drifts and is consistent with the correlation-based alignment procedure outlined in Doroshenko et al. (2020). We conclude therefore that, despite uncertainty in the orbital parameters of the system and rapid observed spin-up, the observed spin-frequency evolution implies that the sharp peak around phase 0.5 is indeed the same feature in both IXPE observations, and thus their absolute phase alignment obtained above is indeed correct.

3. Results

As with other accreting pulsars observed by IXPE so far (Doroshenko et al. 2022; Tsygankov et al. 2023; Mushtukov et al. 2023; Malacaria et al. 2023; Forsblom et al. 2023), the average polarization in the 2−8 keV band observed from the source is low. We measured a PD of $4.4\% \pm 0.2\%$ at PA $= 79^\circ \pm 2^\circ$ in Obs. 1 and PD $= 4.9\% \pm 0.2\%$, PA $= -59^\circ \pm 2^\circ$ in Obs. 2 (uncertainties here and throughout the manuscript are reported at a 1σ confidence level unless stated otherwise). More interesting is the pulse-phase dependence of the observed polarization properties. As a subsequent step, therefore, we conducted a phase-resolved polarimetric analysis. The results for both observations are presented in Fig. 3. We also verified that spectro-polarimetric analysis with XSPEC (Arnaud 1996) using a simple absorbed Comptonization model (`comptt` with parameters similar to those reported by Salganik et al. 2023a for the soft component) gives consistent results, only weakly affected by the assumed spectral model. The motivation for the choice of the binned analysis over spectro-polarimetry is discussed below in Sect. 4. The polarization is detected with a significance exceeding 3σ in 14 out of 16 phase bins in Obs. 1, and in all 32 phase bins of Obs. 2. The higher quality of the data in the latter case is related to a significantly longer exposure that allowed us to collect more photons (despite a factor of two lower flux) and a higher average PD.

As is evident from Fig. 3, both the observed pulse profiles and the polarization properties appear to be drastically different between the two observations. The PD is significantly larger in Obs. 2, reaching 25%, while it remains below 15% in Obs. 1. The profile of the PD (see Fig. 3d) exhibits similar features, such as a peak at phase 0.3 and a secondary broad peak at phase 0.7−0.8, while the third peak of the PD at phase 0.4 present in Obs. 2 is not present in Obs. 1. The observed changes in PA phase dependence between the two observations are even more noteworthy. The PA as a function of phase not only appears to be in antiphase in the two observations, but the amplitude of variations also changes by a factor of two. Another important point one could make here is the remarkable comparative simplicity of the PA phase dependence in both observations, especially in the second one (see Fig. 3e). This can be contrasted with the complex pulse profile that exhibits multiple peaks varying with energy (see Fig. 3a) and also significantly differs between the two observations (even if some common features such as narrow peaks at phases ∼0.3, 0.5 and 0.7 and dips around phases 0.6 and 0.9 can be identified). It is also worth noting that the absolute flux around the pulse minimum remains almost constant whereas the maximum flux changes significantly. As a consequence, the pulsed fraction decreases from ∼66% in Obs. 1 to ∼56% in Obs. 2, remaining, nevertheless, unusually high (see also Salganik et al. 2023b). On the other hand, the PA exhibits in both cases almost sinusoidal modulation with no extra features despite the statistics being definitively sufficient for them to be detected.

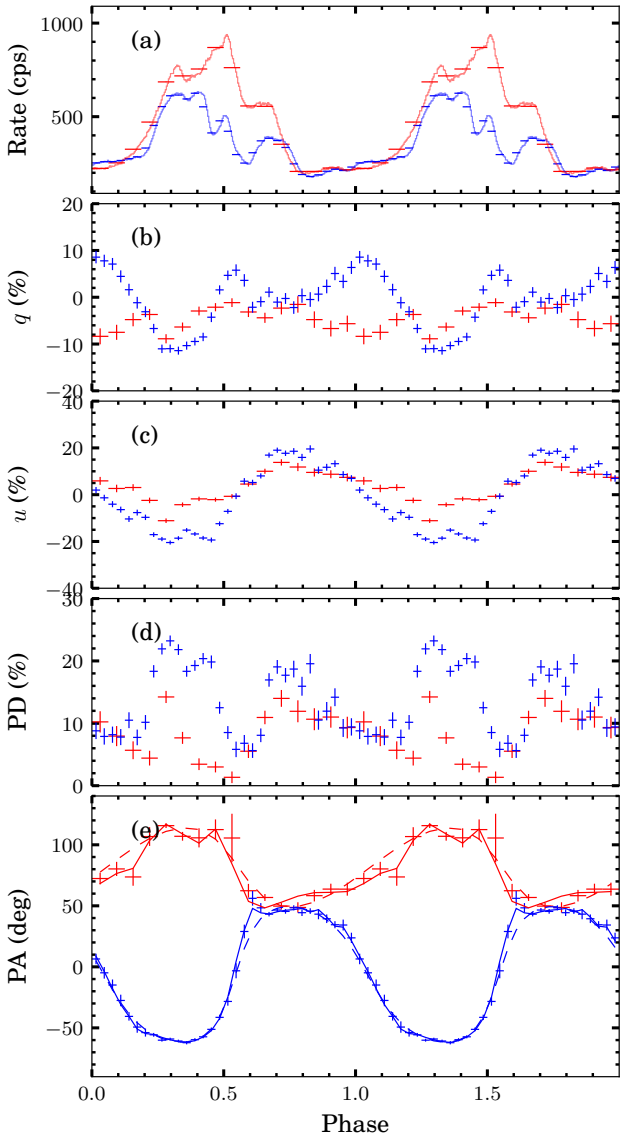

Fig. 3. Pulse-phase dependence of the source flux, the normalized Stokes parameters $q = Q/I$ and $u = U/I$, the PD, and the PA for the first (red) and second (blue) IXPE observations, respectively. In panel e, the lines show the RVM best-fit model for each observation individually with no extra components (dashed, Sect. 4.1) and a joint fit including a constant polarization component (solid, Sect. 4.2).

4. Modeling

The dramatic changes observed in pulse-profile shape and polarization properties are, in fact, not totally unexpected given the likely transition to the supercritical accretion regime (Salganik et al. 2023b) and definitively deserve more detailed analysis. Considering the lack of reliable model predictions for the PD, we focus below mainly on the analysis of the PA phase dependence.

4.1. Rotating vector model

The remarkably simple evolution of the PA with pulse phase ϕ observed up to now with IXPE (Doroshenko et al. 2022; Tsygankov et al. 2022, 2023) is likely related to the alignment of the PA to the projection of the magnetic dipole on the sky due to vacuum polarization (Gnedin et al. 1978; Pavlov & Shibanov 1979;

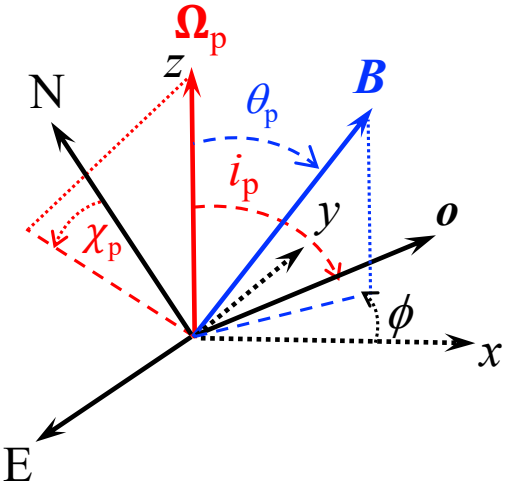

Fig. 4. Geometry of the pulsar and main parameters of the RVM. The pulsar angular momentum, $\mathbf{\Omega}_p$, makes an angle i_p with respect to the line of sight (along vector $\boldsymbol{o}$). The angle θ_p is between magnetic dipole, $\boldsymbol{B}$, and the NS angular momentum $\mathbf{\Omega}_p$. Pulsar phase ϕ is the azimuthal angle of vector $\boldsymbol{B}$ in the plane (x, y) perpendicular to $\mathbf{\Omega}_p$. The position angle χ_p is the angle measured counterclockwise between the direction to the north N and the projection of $\mathbf{\Omega}_p$ on the plane of the sky (N-E).

Heyl & Shaviv 2000; Doroshenko et al. 2022; González-Caniulef et al. 2023). This allowed us to constrain the basic geometry (see Fig. 4) of the pulsar using the rotating vector model (RVM; Radhakrishnan & Cooke 1969; Poutanen 2020):

$$\tan(\chi - \chi_p) = \frac{-\sin\theta_p \ \sin[2\pi(\phi - \phi_p)]}{\sin i_p \cos\theta_p - \cos i_p \sin\theta_p \cos[2\pi(\phi - \phi_p)]}. \quad (1)$$

Here $\chi(\phi)$ is the prediction of the RVM for the PA, χ_p is the position angle (measured counterclockwise from the direction to the north) of the pulsar angular momentum, $i_p \in (0°, 180°)$ is the inclination of the pulsar spin to the line of sight, $\theta_p \in (0°, 90°)$ is the angle between the magnetic dipole and the spin axis, and $\phi_p \in (0, 1)$ is the phase when the northern magnetic pole is closest to the observer.

Considering the rather different PA phase dependence in both observations, we first applied this model to each observation separately using the same Markov chain Monte Carlo (MCMC) procedure as in Doroshenko et al. (2022), directly fitting observed PA values in individual phase bins. The best-fit model to the PA data is depicted in Fig. 3e. The corner plots (Foreman-Mackey 2016) characterizing the interdependence of model parameters and showing their best-fit values are presented in Fig. 5. The agreement of the best-fit model with the data is striking, particularly for Obs. 2, where the data quality is the best among all pulsars observed to date by IXPE. Indeed, there are only minor residuals around phase 0.6 corresponding to minimal PD values and thus having the lowest significance.

On the other hand, direct comparison of the obtained RVM parameters for the two observations implies significantly different pulsar geometry, which was not really expected. First, we see a rather dramatic change in the pulsar position angle, χ_p, by roughly 90°. This change might not mean that the pulsar has turned by 90° on the sky, but could also result from the polarization-mode switch from X to O or vice versa. Second, there appears to be a large change in the pulsar inclination, i_p, which varies from 50° to 70° in Obs. 1 to about 100° in Obs. 2. The apparent change in the χ_p value is also

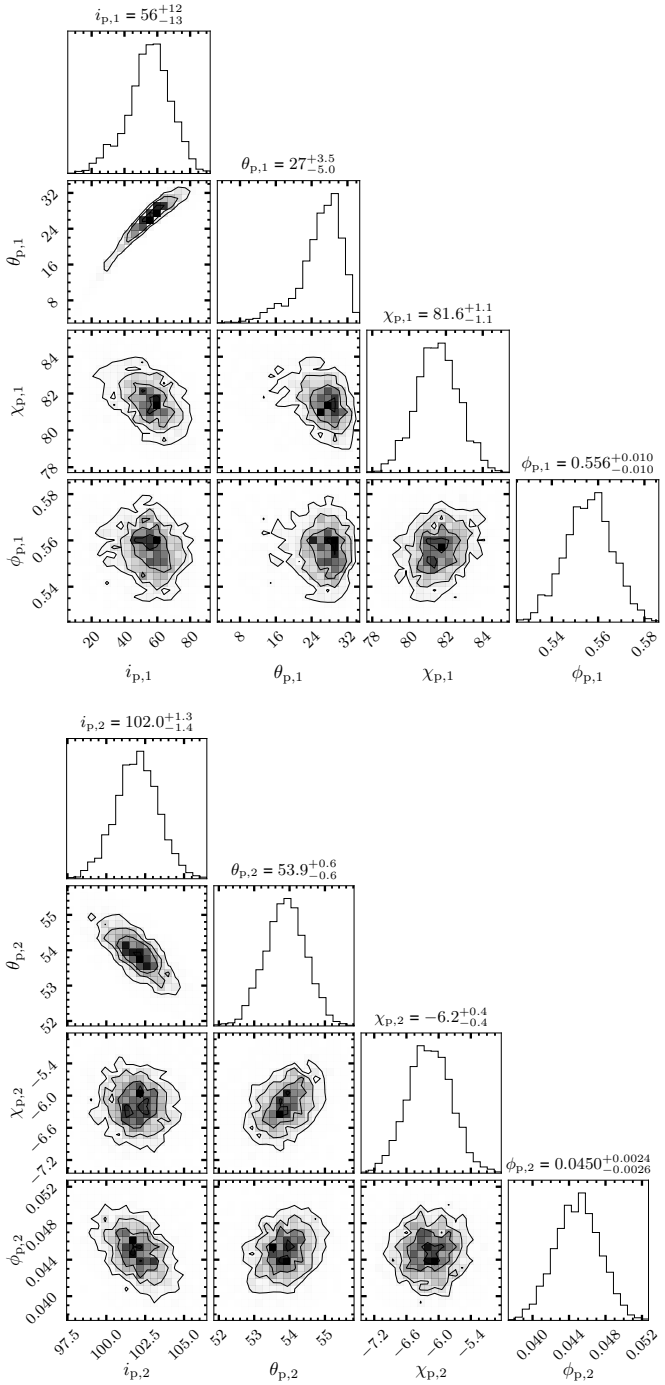

Fig. 5. Corner plots for the RVM fit for each observation individually without additional components. The results for Obs. 1 (top) and Obs. 2 (bottom) are shown. RVM parameters i_p, θ_p, and χ_p are in degrees.

accompanied by the change of the zero phase, ϕ_p, by half a period. Finally, the magnetic obliquity, θ_p, has changed from ~30° to ~54°. While the transition from supercritical to subcritical accretion regime (Salganik et al. 2023b) could be expected to lead to a switch of the dominant polarization mode, it does not explain the significant changes observed at other angles. We emphasize that the fact that the observed PA variations are well described by a RVM implies that the PA is defined by the magnetic field structure at the polarization radius (Doroshenko et al. 2022) and thus is likely unrelated to local changes in

emission-region geometry. On the other hand, it is, of course, difficult to imagine the orientation of the neutron star changing on such a short timescale. Moreover, time-resolved analysis similar to that described above revealed no significant geometry changes within either observation. We considered, therefore, an alternative explanation to the very peculiar behavior of the PA.

4.2. Two-component polarization model

Given the observed changes in the spectral hardness (Salganik et al. 2023b) and pulse profiles, the potential presence of an additional polarized component with different properties in one or both observations could be considered as a natural explanation. We attempted, therefore, to single out this component using the spectro-polarimetric analysis of IXPE data. Unfortunately, we found that the results are inconclusive. This is mainly due to the fact that the available 2−8 keV spectra do not allow one to reliably disentangle the broad continuum components reported by Salganik et al. (2023b); consequently, it it necessary to undertake broadband spectro-polarimetric analysis to get meaningful results. A joint analysis of IXPE, NICER, SRG/ART-XC, and Insight-HXMT data is ongoing and will be reported elsewhere. However, some estimates can be obtained by using binned IXPE products alone, as we discuss below.

Plotting Stokes parameters on the (q, u) plane, we realized that there is a certain similarity between the two observations, but the amplitude of the variations is larger in Obs. 2 and the data points are shifted relative to each other. This supports the idea that, in addition to the polarized radiation coming from the pulsar directly, there is a component that does not depend on phase (or at least depends less on it than the variable pulsar component). A similar conclusion could be reached if one considers the "off-pulse" as background in both observations (i.e., resulting in a more similar phase dependence for both the PD and PA). We attempted, therefore, to disentangle the two components through modeling of the observed Stokes parameters. This can be done by expressing the absolute Stokes parameters for each observation as a sum of the variable component described by the RVM and an additional constant component:

$$\begin{aligned} I(\phi) &= I_\mathrm{c} + I_\mathrm{p}(\phi), \\ Q(\phi) &= Q_\mathrm{c} + P_\mathrm{p}(\phi) I_\mathrm{p}(\phi) \cos[2\chi(\phi)], \\ U(\phi) &= U_\mathrm{c} + P_\mathrm{p}(\phi) I_\mathrm{p}(\phi) \sin[2\chi(\phi)]. \end{aligned} \tag{2}$$

By I, Q, and U, we can assume here that the observed Stokes parameters are normalized to the average flux value with indices denoting the constant (c) and pulsed (p) components, P_p is the PD of the variable component, and its PA χ is given by Eq. (1). The Stokes parameters $(Q_\mathrm{c}, U_\mathrm{c})$ are related to the PD, P_c, and the flux, I_c, of the constant component,

$$Q_\mathrm{c} = P_\mathrm{c} I_\mathrm{c} \cos(2\chi_\mathrm{c}), \quad U_\mathrm{c} = P_\mathrm{c} I_\mathrm{c} \sin(2\chi_\mathrm{c}), \tag{3}$$

with its PA being $\chi_\mathrm{c} = (1/2)\arctan(U_\mathrm{c}/Q_\mathrm{c})$. The polarized flux of the variable component was computed as

$$P_\mathrm{p} I_\mathrm{p}(\phi) = \sqrt{[Q(\phi) - Q_\mathrm{c}]^2 + [U(\phi) - U_\mathrm{c}]^2}. \tag{4}$$

The expected PD and PA of the total emission could then be obtained from the summed Stokes parameters of both components and could be compared with the observed values. The null hypothesis is now that the geometry of the pulsar does not change between the observations and the observed changes in the polarization properties are related to the presence of an additional, unpulsed, polarized component. This means that a single RVM could fit the variable PA(ϕ) for both observations.

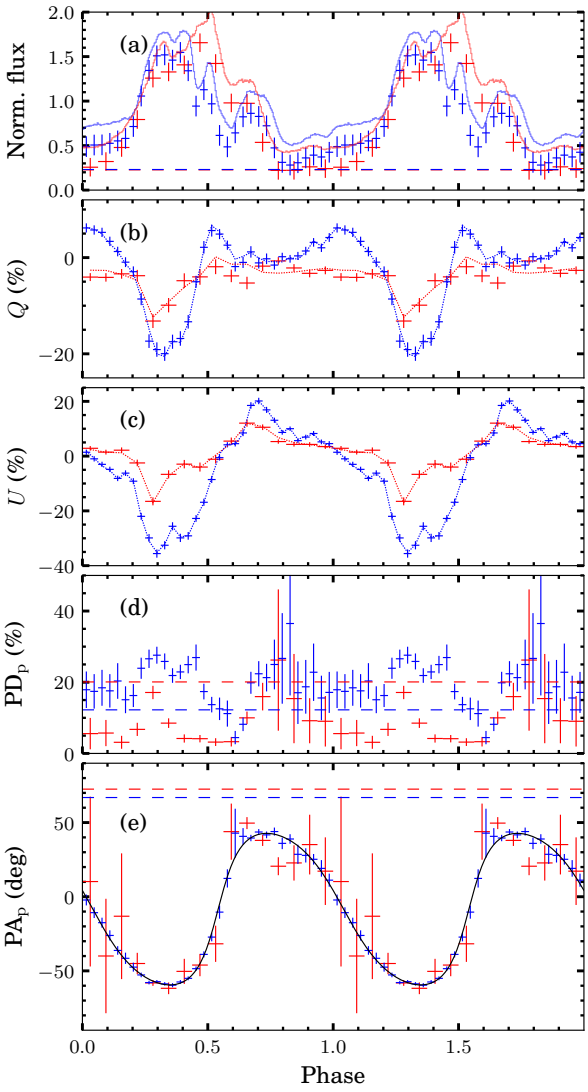

Fig. 6. Results for the two-component model corresponding to the best-fit parameters listed in Fig. 7. Panel a shows the total normalized flux (solid lines), the mean value for the constant component ($I_{\mathrm{c},1} = I_{\mathrm{c},2} = 0.23$, horizontal dashed lines), and the flux of the variable component accounting for the uncertainty in the constant component (crosses). Panels b and c show the observed Stokes parameters normalized to the average flux (crosses) and the best-fit model (dotted lines). Panels d and e show the PD and PA for constant (horizontal dashed lines) and variable (crosses) components, respectively. The solid line in panel e matches the solid set of lines in Fig. 3e with the constant component subtracted. Red and blue symbols and lines correspond to Obs. 1 and Obs. 2, respectively.

In practice, this can be done by including six additional parameters $(I_{\mathrm{c},i}, Q_{\mathrm{c},i}, U_{\mathrm{c},i})$ corresponding to the Stokes parameters (normalized to the average flux) of the constant component in two observations ($i = 1, 2$) in the model so that the right part of Eq. (2) is fully defined. The four RVM parameters and $(I_{\mathrm{c},i}, Q_{\mathrm{c},i}, U_{\mathrm{c},i})$ can then be estimated by comparing the model prediction with the observed Q, U values. In this case modeling is done directly in Q, U space, so observed PA or PD values are not used directly. To obtain model parameters and their uncertainties, we used MCMC sampling as implemented in the

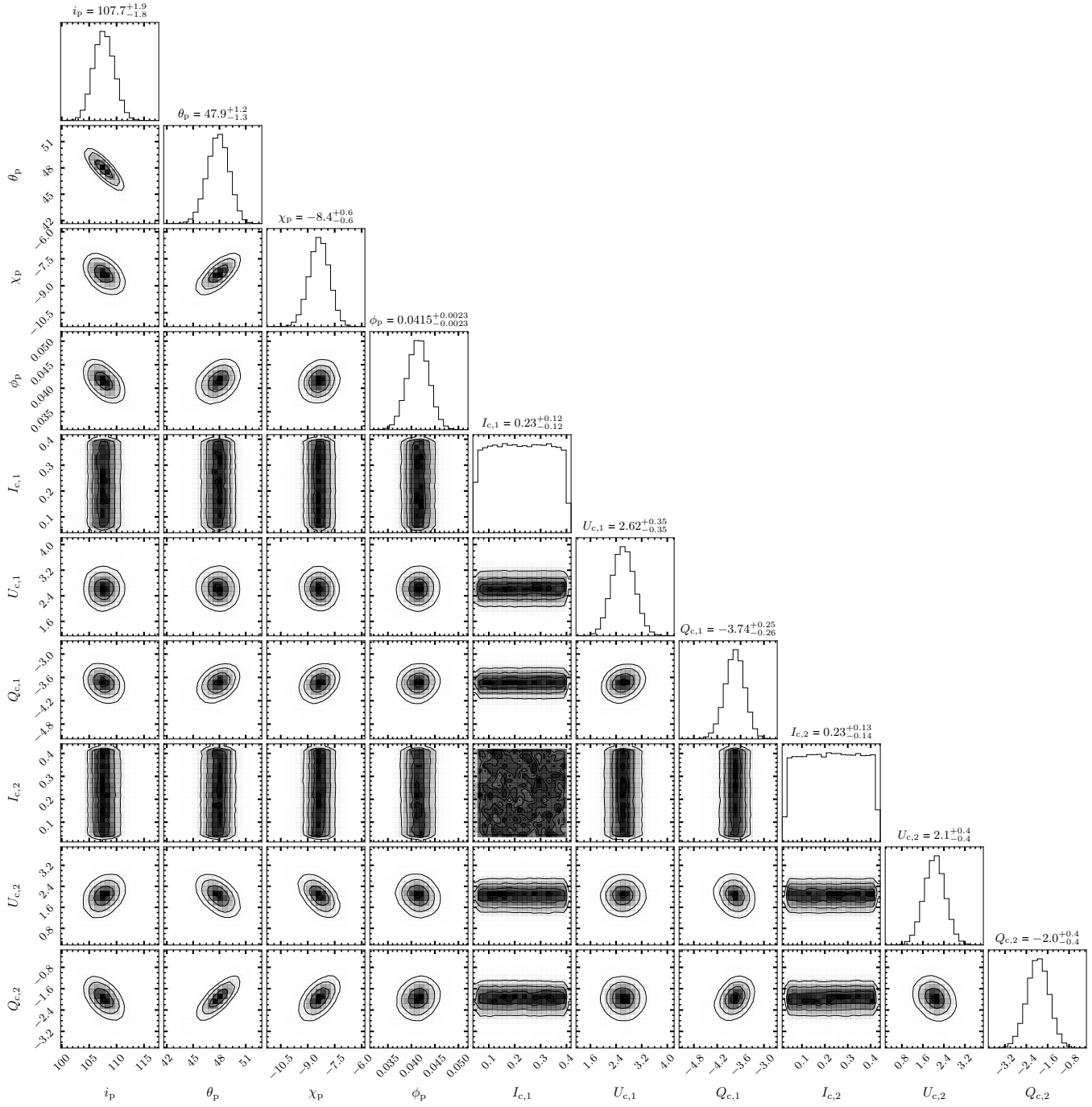

Fig. 7. Corner plots for the simultaneous fit of both observations including the unpulsed polarization component contribution (parameters correspond to a set of solid lines in Fig. 3e and lines in Fig. 6). The RVM parameters i_p, θ_p, and χ_p are in degrees. The Stokes parameters $Q_{c,i}$ and $U_{c,i}$ are expressed in percent of the average flux, while $I_{c,i}$ are fractions of the average flux. The uncertainties are reported at a 1σ confidence level.

EMCEE package (Foreman-Mackey et al. 2013), assuming uniform priors for all parameters except for i_p and θ_p, where flat priors for cosine of the angles were assumed. The likelihood was calculated using χ^2 statistics for Q, U (as the uncertainties of the observed Stokes parameters are normally distributed), and set to negative infinity for parameters outside of ranges defined above for the RVM and for $P_c > 1$ and $P_p(\phi) > 1$ to account for prior knowledge of their possible values. The results are presented in Figs. 6 and 7.

We emphasize that the main role in the analysis above is played by the Stokes parameters Q_c, U_c (normalized to the averaged flux) of the constant component. The obtained RVM parameters $i_p = 108° \pm 2°$, $\theta_p = 48° \pm 1°$, $\chi_p = -8.^{\circ}4 \pm 0.^{\circ}6$, and $\phi_p = 0.041 \pm 0.002$ do not depend at all on the assumption about I_c and they are well constrained within the framework of the adopted two-component polarization model. From the best-fit Stokes parameters of the constant component of $Q_{c,1} = -3.7\% \pm 0.3\%$, $U_{c,1} = 2.6\% \pm 0.3\%$ and $Q_{c,2} = -2.0\% \pm 0.4\%$, $U_{c,2} = 2.1\% \pm 0.4\%$, we can get its PAs, $\chi_{c,1} = 72° \pm 2°$ and $\chi_{c,2} = 67° \pm 4°$, and the polarized fluxes, $P_{c,i}I_{c,i} = \sqrt{Q^2_{c,i} + U^2_{c,i}}$ of $4.5\% \pm 0.3\%$ and $2.9\% \pm 0.4\%$, for the two observations, respectively. The data allowed us to constrain the polarized flux of the constant component, whereas the flux and the PD

separately cannot be well determined. The limits on $I_{c,i}$ only appear because the PDs of both components, P_c and P_p, need to be less than 100%. This condition translates to the limits on the flux of the constant component, $I_c \geq P_c I_c$ and $I_c \leq \min[I(\phi) - P_p(\phi)I_p(\phi)]$, as is apparent in Fig. 7. The resulting limits are $I_{c,1} \in [0.038, 0.42]$ for Obs. 1 and $I_{c,2} \in [0.013, 0.44]$ for Obs. 2. For the maximum possible I_c, we get the minimum possible $P_{c,1} \approx 12\%$ and $P_{c,2} \approx 7\%$, and P_c grows inversely proportional to I_c. For example, for the mean $I_c = 0.23$, we get $P_{c,1} \approx 20\%$ and $P_{c,2} \approx 12.5\%$.

These estimates are relevant for discussion of the physical origin of the constant component. Indeed, to remain independent of the pulse phase, the constant component must originate far from the neutron star. Possible sites include reprocessing in the matter piled up at the magnetosphere, reflection from the accretion disk or in the disk winds, scattering in the circumbinary disk of the Be star, or reprocessing in the atmosphere of the donor star itself. The fraction of reprocessed light is, however, on the order of 20%. This is relatively high, so the origin of the component must be able to explain it, which favors locations relatively close to the pulsar, such as the magnetosphere and/or the accretion disk. Considering the growing evidence for the presence of outflows launched from inner regions of the accretion disk of BeXRBs during both Type I and Type II outbursts (Jaisawal et al. 2019; van den Eijnden et al. 2019, 2022; Chatzis et al. 2022) and an expected non-negligible effect on pulse profiles and spectra at higher accretion rates (Mushtukov & Portegies Zwart 2023), scattering in a highly ionized equatorial disk wind seems to be a plausible scenario. It has also been suggested that reprocessing in the inner disk regions and disk wind is responsible for the soft excess observed in many transient XRPs (Hickox et al. 2004), including RX J0440.9+4431 (Salganik et al. 2023b), for which the soft excess was also found to be more prominent at higher luminosities. Larger deviations from the RVM and the higher PD of the constant component in Obs. 1, where the accretion rate and likely the outflow rate were higher, is also in line with this hypothesis. For an idealized case in which the scattering material lies in a plane, the polarization of the scattered component depends on the inclination to the plane normal, i, as $\mathrm{PD} = \sin^2 i/(3 - \cos^2 i)$ (Sunyaev & Titarchuk 1985), reaching 33% edge-on, and is still larger than 30% for $i > 66°$. For a wind occupying a larger solid angle, the PD drops, but even for the half-opening of the wind (measured from the orbital plane) of 30° (i.e., occupying half of the sky as seen from the pulsar), the PD drops by just a factor of 0.77, being above 22% for $i > 66°$. These estimates of the PD are comparable to the data. The contribution of the scattered emission to the total flux in the soft band can also be appreciable, reaching at least 10% at higher accretion rates (Jaisawal et al. 2019). More accurate constraints on the fraction of scattered light and polarization of the scattered component can also be obtained through broadband spectral analysis and detailed modeling of scattering and fluorescent lines in the vicinity of the pulsar.

We note also that a high estimated value of pulsar inclination suggests that the accretion disk is likely being viewed close to edge-on, which is expected to yield the largest polarization. We note that in this scenario the PA of the constant component is expected to be aligned with the position angle of the normal to the accretion disk and the orbital plane, and thus is not expected to change with the orbital phase, which is consistent with observations. The orientation of the accretion disk relative to the decretion disk of the Be star can be tested through optical polarimetric observations. Preliminary analysis of data obtained as part of our optical polarimetric campaign with the DIPol-2 high-precision polarimeter (Piirola et al. 2014) at the T60 telescope at Haleakala Observatory yields a PA of the intrinsic optical polarization of 55°−71° (Nitindala et al., in prep.). Such a close agreement with the X-ray PA does not look like a coincidence and probably implies that the pulsar orbit lies close to the decretion-disk plane.

It is interesting to discuss the phase dependence of the variable component. First, one can note that $\phi_p = 0$ corresponds to the northern pole coming close to the observer, while at $\phi_p = 0.5$ the southern pole is close. For the estimated $i_p = 108°$ and $\theta_p = 48°$, the minimum angles between the normal to the spots and the line of sight are $i_p - \theta_p = 60°$ and $180° - \theta_p - i_p = 24°$, respectively. Thus, it is not surprising that the flux has a maximum when the southern spot is closer to the observer in both observations.

5. Summary and conclusions

We have presented the first results of IXPE observations of the 2023 Type II outburst of the bright Be transient, RX J0440.9+4431. The observations were carried out at two luminosity levels and likely captured the object in two accretion regimes associated with the presence and absence of an accretion column (Basko & Sunyaev 1976; Salganik et al. 2023b). This presented a unique opportunity to probe the changes in emission-region geometry and radiative processes related to the onset of an accretion column by means of pulse-phase-resolved X-ray polarimetry.

Our analysis indeed revealed that the source is strongly polarized in both observations, with the PD exceeding 20% in some phase bins. The observed PA phase dependence remains remarkably consistent with the predictions from the RVM model (Radhakrishnan & Cooke 1969; Poutanen 2020), but the derived geometrical parameters appear to be completely different for the two observations. While the observed 90° jump in the pulsar spin position angle could be attributed to a change in the dominant polarization mode associated with the transition, there is no obvious explanation for changes in other angles that amount to tens of degrees on a timescale of just a few days. It is difficult to imagine that such changes are associated with a true change in the orientation of the neutron star's spin and magnetic axes with respect to the observer. That led us to consider alternative explanations, in particular the potential presence of an additional polarized component.

We find that the observed PA phase dependence in both observations can indeed be described with no changes in pulsar geometry if a strongly polarized ($\mathrm{PD} \sim 10$–30%, $\mathrm{PA} \approx 70°$) unpulsed component is present. Subtracting the Stokes parameters of the constant component from the observed ones, we have derived constraints on the pulsar geometry, obtaining a pulsar inclination of $i_p \approx 108°$, a magnetic obliquity of $\theta_p \approx 48°$, and a position angle of the pulsar spin of $\chi_p \approx -8.^\circ4$. Properties of the unpulsed component (e.g., its contribution to the total flux, the PD, and the PA) appear to be roughly constant between the two observations. We suggest that this component can be produced by scattering the pulsar radiation in a highly ionized disk wind. The observed PA phase dependence is consistent, and for Obs. 2 shows almost perfect agreement, with the simple RVM model used up to now to study the geometry of XRPs. Yet, despite formal agreement, a more detailed analysis of the two observations carried out at different epochs reveals that the situation is far more complicated. It cannot be excluded that similar complications might be relevant for studies of other XRPs observed by IXPE. We conclude, therefore, that the importance of high-quality, multi-epoch polarimetric

observations, preferably accompanied by broadband spectroscopic and optical polarimetric observations, should not be underestimated.

Acknowledgements. The Imaging X-ray Polarimetry Explorer (IXPE) is a joint US and Italian mission. The US contribution is supported by the National Aeronautics and Space Administration (NASA) and led and managed by its Marshall Space Flight Center (MSFC), with industry partner Ball Aerospace (contract NNM15AA18C). The Italian contribution is supported by the Italian Space Agency (Agenzia Spaziale Italiana, ASI) through contract ASI-OHBI-2017-12-I.0, agreements ASI-INAF-2017-12-H0 and ASI-INFN-2017.13-H0, and its Space Science Data Center (SSDC) with agreements ASI-INAF-2022-14-HH.0 and ASI-INFN 2021-43-HH.0, and by the Istituto Nazionale di Astrofisica (INAF) and the Istituto Nazionale di Fisica Nucleare (INFN) in Italy. This research used data products provided by the IXPE Team (MSFC, SSDC, INAF, and INFN) and distributed with additional software tools by the High-Energy Astrophysics Science Archive Research Center (HEASARC), at NASA Goddard Space Flight Center (GSFC). We acknowledge support from the German Academic Exchange Service (DAAD) travel grant 57525212 (VD, VFS), the Academy of Finland grants 333112, 349144, 349373, and 349906 (JP, SST, SVF), the Natural Sciences and Engineering Research Council of Canada (NSERC) and the Canadian Space Agency (JH), the Väisälä Foundation (SST), UKRI Stephen Hawking fellowship (AAM), the German Research Foundation (DFG) grant WE 1312/59-1 (VFS), the Vilho, Yrjö and Kalle Väisälä Foundation, and Suomen Kulttuurirahasto (VK).

References

Arnaud, K. A. 1996, in Astronomical Data Analysis Software and Systems V, eds. G. H. Jacoby, & J. Barnes, ASP Conf. Ser., 101, 17
Bailer-Jones, C. A. L., Rybizki, J., Fouesneau, M., Demleitner, M., & Andrae, R. 2021, AJ, 161, 147
Baldini, L., Barbanera, M., Bellazzini, R., et al. 2021, Astropart. Phys., 133, 102628
Baldini, L., Bucciantini, N., Di Lalla, N., et al. 2022, SoftwareX, 19, 101194
Basko, M. M., & Sunyaev, R. A. 1976, MNRAS, 175, 395
Chatzis, M., Petropoulou, M., & Vasilopoulos, G. 2022, MNRAS, 509, 2532
Coley, J. B., Gendreau, K., Pottschmidt, K., et al. 2023, ATel, 15907, 1
Deeter, J. E., Boynton, P. E., & Pravdo, S. H. 1981, ApJ, 247, 1003
Di Marco, A., Soffitta, P., Costa, E., et al. 2023, AJ, 165, 143
Doroshenko, V., Zhang, S. N., Santangelo, A., et al. 2020, MNRAS, 491, 1857
Doroshenko, V., Poutanen, J., Tsygankov, S. S., et al. 2022, Nat. Astron., 6, 1433
Ferrigno, C., Farinelli, R., Bozzo, E., et al. 2013, A&A, 553, A103
Finger, M. H., & Camero-Arranz, A. 2010, ATel, 2537, 1
Foreman-Mackey, D. 2016, J. Open Sour. Softw., 1, 24
Foreman-Mackey, D., Hogg, D. W., Lang, D., & Goodman, J. 2013, PASP, 125, 306
Forsblom, S. V., Poutanen, J., Tsygankov, S. S., et al. 2023, ApJ, 947, L20
Gnedin, Y. N., Pavlov, G. G., & Shibanov, Y. A. 1978, Sov. Astron. Lett., 4, 117
González-Caniulef, D., Caiazzo, I., & Heyl, J. 2023, MNRAS, 519, 5902
Heyl, J. S., & Shaviv, N. J. 2000, MNRAS, 311, 555
Hickox, R. C., Narayan, R., & Kallman, T. R. 2004, ApJ, 614, 881
Jaisawal, G. K., Wilson-Hodge, C. A., Fabian, A. C., et al. 2019, ApJ, 885, 18
Kislat, F., Beilicke, M., Guo, Q., Zajczyk, A., & Krawczynski, H. 2015, Astropart. Phys., 64, 40
La Palombara, N., Sidoli, L., Esposito, P., Tiengo, A., & Mereghetti, S. 2012, A&A, 539, A82
Malacaria, C., Jenke, P., Roberts, O. J., et al. 2020, ApJ, 896, 90
Malacaria, C., Heyl, J., Doroshenko, V., et al. 2023, A&A, 675, A29
Morii, M., Kawai, N., Sugimori, K., et al. 2010, ATel, 2527, 1
Motch, C., Haberl, F., Dennerl, K., Pakull, M., & Janot-Pacheco, E. 1997, A&A, 323, 853
Mushtukov, A. A., & Portegies Zwart, S. 2023, MNRAS, 518, 5457
Mushtukov, A. A., Tsygankov, S. S., Poutanen, J., et al. 2023, MNRAS, 524, 2004
Nakajima, M., Negoro, H., Mihara, T., et al. 2022, ATel, 15835, 1
Pal, S., Mandal, M., Gendreau, K., et al. 2023, ATel, 15868, 1
Pavlov, G. G., & Shibanov, Y. A. 1979, Sov. J. Exp. Theor. Phys., 49, 741
Piirola, V., Berdyugin, A., & Berdyugina, S. 2014, Proc. SPIE, 9147, 91478I
Poutanen, J. 2020, A&A, 641, A166
Radhakrishnan, V., & Cooke, D. J. 1969, Astrophys. Lett., 3, 225
Reig, P., & Nespoli, E. 2013, A&A, 551, A1
Reig, P., & Roche, P. 1999, MNRAS, 306, 100
Reig, P., Negueruela, I., Fabregat, J., Chato, R., & Coe, M. J. 2005, A&A, 440, 1079
Salganik, A., Tsygankov, S. S., Lutovinov, A. A., & Molkov, S. V. 2023a, ATel, 15874, 1
Salganik, A., Tsygankov, S. S., Doroshenko, V., et al. 2023b, MNRAS, 524, 5213
Soffitta, P., Baldini, L., Bellazzini, R., et al. 2021, AJ, 162, 208
Sunyaev, R. A., & Titarchuk, L. G. 1985, A&A, 143, 374
Tsygankov, S. S., Krivonos, R. A., & Lutovinov, A. A. 2012, MNRAS, 421, 2407
Tsygankov, S. S., Mushtukov, A. A., Suleimanov, V. F., et al. 2017, A&A, 608, A17
Tsygankov, S. S., Doroshenko, V., Poutanen, J., et al. 2022, ApJ, 941, L14
Tsygankov, S. S., Doroshenko, V., Mushtukov, A. A., et al. 2023, A&A, 675, A48
Usui, R., Morii, M., Kawai, N., et al. 2012, PASJ, 64, 79
van den Eijnden, J., Degenaar, N., Schulz, N. S., et al. 2019, MNRAS, 487, 4355
van den Eijnden, J., Degenaar, N., Russell, T. D., et al. 2022, MNRAS, 516, 4844
Weisskopf, M. C., Soffitta, P., Baldini, L., et al. 2022, J. Astron. Telesc. Instrum. Syst., 8, 026002
Wilson-Hodge, C. A., Malacaria, C., Jenke, P. A., et al. 2018, ApJ, 863, 9

[1] Institut für Astronomie und Astrophysik, Universität Tübingen, Sand 1, 72076 Tübingen, Germany
e-mail: doroshv@astro.uni-tuebingen.de
[2] Department of Physics and Astronomy, University of Turku, 20014 Turku, Finland
[3] University of British Columbia, Vancouver BC V6T 1Z4, Canada
[4] Division of Physics, Mathematics and Astronomy, California Institute of Technology, Pasadena, CA 91125, USA
[5] Dipartimento di Fisica e Astronomia, Università degli Studi di Padova, Via Marzolo 8, 35131 Padova, Italy
[6] Mullard Space Science Laboratory, University College London, Holmbury St Mary, Dorking, Surrey RH5 6NT, UK
[7] Nordita, KTH Royal Institute of Technology and Stockholm University, Hannes Alfvéns väg 12, 106 91 Stockholm, Sweden
[8] NASA Marshall Space Flight Center, Huntsville, AL 35812, USA
[9] Institut de Recherche en Astrophysique et Planétologie, UPS-OMP, CNRS, CNES, 9 Avenue du Colonel Roche, BP 44346 31028 Toulouse Cedex 4, France
[10] International Space Science Institute, Hallerstrasse 6, 3012 Bern, Switzerland
[11] Astrophysics, Department of Physics, University of Oxford, Denys Wilkinson Building, Keble Road, Oxford OX1 3RH, UK
[12] Space Research Institute (IKI) of the Russian Academy of Sciences, Profsoyuznaya Str. 84/32, Moscow 117997, Russia
[13] Department of Astrophysics, St. Petersburg State University, Universitetsky Pr. 28, Petrodvoretz, 198504 St. Petersburg, Russia
[14] Instituto de Astrofísicade Andalucía – CSIC, Glorieta de la Astronomía s/n, 18008 Granada, Spain
[15] INAF – Osservatorio Astronomico di Roma, Via Frascati 33, 00040 Monte Porzio Catone, RM, Italy
[16] Space Science Data Center, Agenzia Spaziale Italiana, Via del Politecnico snc, 00133 Roma, Italy
[17] INAF – Osservatorio Astronomico di Cagliari, Via della Scienza 5, 09047 Selargius, CA, Italy
[18] Istituto Nazionale di Fisica Nucleare, Sezione di Pisa, Largo B. Pontecorvo 3, 56127 Pisa, Italy
[19] Dipartimento di Fisica, Università di Pisa, Largo B. Pontecorvo 3, 56127 Pisa, Italy
[20] Dipartimento di Matematica e Fisica, Università degli Studi Roma Tre, Via della Vasca Navale 84, 00146 Roma, Italy
[21] Istituto Nazionale di Fisica Nucleare, Sezione di Torino, Via Pietro Giuria 1, 10125 Torino, Italy
[22] Dipartimento di Fisica, Università degli Studi di Torino, Via Pietro Giuria 1, 10125 Torino, Italy
[23] INAF Osservatorio Astrofisico di Arcetri, Largo Enrico Fermi 5, 50125 Firenze, Italy
[24] Dipartimento di Fisica e Astronomia, Università degli Studi di Firenze, Via Sansone 1, 50019 Sesto Fiorentino, FI, Italy
[25] Istituto Nazionale di Fisica Nucleare, Sezione di Firenze, Via Sansone 1, 50019 Sesto Fiorentino, FI, Italy
[26] Agenzia Spaziale Italiana, Via del Politecnico snc, 00133 Roma, Italy
[27] Science and Technology Institute, Universities Space Research Association, Huntsville, AL 35805, USA

[28] Istituto Nazionale di Fisica Nucleare, Sezione di Roma "Tor Vergata", Via della Ricerca Scientifica 1, 00133 Roma, Italy
[29] INAF – Istituto di Astrofisica e Planetologia Spaziali, Via del Fosso del Cavaliere 100, 00133 Roma, Italy
[30] Department of Physics and Kavli Institute for Particle Astrophysics and Cosmology, Stanford University, Stanford, CA 94305, USA
[31] Astronomical Institute of the Czech Academy of Sciences, Boční II 1401/1, 14100 Praha 4, Czech Republic
[32] RIKEN Cluster for Pioneering Research, 2-1 Hirosawa, Wako, Saitama 351-0198, Japan
[33] California Institute of Technology, Pasadena, CA 91125, USA
[34] Yamagata University, 1-4-12 Kojirakawa-machi, Yamagata-shi 990-8560, Japan
[35] Osaka University, 1-1 Yamadaoka, Suita, Osaka 565-0871, Japan
[36] International Center for Hadron Astrophysics, Chiba University, Chiba 263-8522, Japan
[37] Institute for Astrophysical Research, Boston University, 725 Commonwealth Avenue, Boston, MA 02215, USA
[38] Department of Physics and Astronomy and Space Science Center, University of New Hampshire, Durham, NH 03824, USA
[39] Physics Department and McDonnell Center for the Space Sciences, Washington University in St. Louis, St. Louis, MO 63130, USA
[40] Finnish Centre for Astronomy with ESO, University of Turku, 20014 Turku, Finland
[41] Istituto Nazionale di Fisica Nucleare, Sezione di Napoli, Strada Comunale Cinthia, 80126 Napoli, Italy
[42] Université de Strasbourg, CNRS, Observatoire Astronomique de Strasbourg, UMR 7550, 67000 Strasbourg, France
[43] MIT Kavli Institute for Astrophysics and Space Research, Massachusetts Institute of Technology, 77 Massachusetts Avenue, Cambridge, MA 02139, USA
[44] Graduate School of Science, Division of Particle and Astrophysical Science, Nagoya University, Furo-cho, Chikusa-ku, Nagoya, Aichi 464-8602, Japan
[45] Hiroshima Astrophysical Science Center, Hiroshima University, 1-3-1 Kagamiyama, Higashi-Hiroshima, Hiroshima 739-8526, Japan
[46] University of Maryland, Baltimore County, Baltimore, MD 21250, USA
[47] NASA Goddard Space Flight Center, Greenbelt, MD 20771, USA
[48] Center for Research and Exploration in Space Science and Technology, NASA/GSFC, Greenbelt, MD 20771, USA
[49] Department of Physics, University of Hong Kong, Pokfulam, Hong Kong
[50] Department of Astronomy and Astrophysics, Pennsylvania State University, University Park, PA 16801, USA
[51] Université Grenoble Alpes, CNRS, IPAG, 38000 Grenoble, France
[52] Center for Astrophysics, Harvard & Smithsonian, 60 Garden St, Cambridge, MA 02138, USA
[53] INAF – Osservatorio Astronomico di Brera, Via E. Bianchi 46, 23807 Merate, LC, Italy
[54] Dipartimento di Fisica, Università degli Studi di Roma "Tor Vergata", Via della Ricerca Scientifica 1, 00133 Roma, Italy
[55] Department of Astronomy, University of Maryland, College Park, MD 20742, USA
[56] Anton Pannekoek Institute for Astronomy & GRAPPA, University of Amsterdam, Science Park 904, 1098 XH Amsterdam, The Netherlands
[57] Guangxi Key Laboratory for Relativistic Astrophysics, School of Physical Science and Technology, Guangxi University, Nanning 530004, PR China